Complex eigenrays algorithm for infrasound propagation in a windy range dependent atmosphere

Annie Zelias, Olaf Gainville, François Coulouvrat

Complex eigenrays algorithm for infrasound propagation in a windy range dependent atmosphere

Annie Zelias,[1, a)] Olaf Gainville,[1] and Francois Coulouvrat[2]

[1)] *CEA, DAM, DIF F-91297 Arpajon, France*

[2)] *Institut Jean le Rond d'Alembert, Sorbonne Universite, UMR CNRS 7190, France*

(Dated: 11 May 2022)

The ray-tracing is a simple and efficient three dimensional method, which reduces the problem of infrasound propagation to a series of one dimensional cases along acoustical rays. However, in relatively frequent cases, infrasound stations are located into geometrical shadow zones, where only diffracted waves are recorded. The corresponding arrivals cannot be predicted by ray theory. To simulate infrasound propagation in these zones, the ray-tracing method is generalized to complex ray theory. The source, the media and the ground parameters are all considered as complex numbers. For applications with realistic atmospheric data including stratified temperature and wind, as well as range-dependency of atmospheric profiles, an efficient algorithm determining complex eigenrays in shadow zones is presented. It is illustrated by a two dimensional case of a point source.

[a)] Also at: Institut Jean le Rond d'Alembert, Sorbonne Universite, UMR CNRS 7190, France

I. INTRODUCTION

Geometrical acoustics is a common method to study long-range infrasound propagation in the atmosphere. It relies on a high frequency approximation applied to fluid mechanics equations (Candel, 1977; Ostashev and Wilson, 2015; Pierce, 1994; Whitham, 1956). It reduces the propagation as a series of one dimensional cases along acoustical rays. This ray-tracing method is attractive because it allows simple and fast computation taking into account 3-D sources, earth orography and atmospheric data (Scott *et al.*, 2017). Nowadays, infrasound propagation and particularly ray tracing, is a reference tool for inversion problems such as source localization (Blom, 2019; Gainville *et al.*, 2017) or atmospheric sounding (Drob *et al.*, 2010; Lalande *et al.*, 2012; Vanderbecken *et al.*, 2020). However, this method leads to the apparition of caustics and shadow zones. Caustics are zones of rays focusing, described by catastrophe theory as amplitude singularities (Thom, 1983). They can be due to either atmospheric refraction or to source motion (Pierce and Maglieri, 1972). In shadow zones no ray penetrates, and the observable pressure field there is due to diffraction (Kulichkov and Golikova, 2013). Shadow zones are related to either caustics or to geometrical discontinuities of the propagation medium, in particular the Earth surface for infrasound.

Infrasound stations of the International Monitoring System network of the Comprehensive Nuclear-Test-Ban Treaty are frequently located into shadow zones (Blixt *et al.*, 2019; de Groot-Hedlin *et al.*, 2010; Evers *et al.*, 2012; Farges *et al.*, 2021; Gainville *et al.*, 2017; Green *et al.*, 2018; Le Pichon *et al.*, 2010; Sabatini *et al.*, 2019).

In order to predict the signal in shadow zone of caustics, several geometrical methods have been proposed. The Maslov summation (Kendall and Thomson, 1993; Kravtsov and Zhu, 2010; Piserchia, 1998; Thomson and Chapman, 1985), takes into account a hybrid space where caustics no longer exists. The uniform theory of diffraction (UTD) computes the field locally around the caustic (Ludwig, 1966; White and Pedersen, 1981). Gaussian beams add a width to rays (Porter and Bucker, 1987). Complex ray theory was first introduced by Keller (1962) with the Geometrical Theory of Diffraction and was used by Kravtsov in optics (Kravtsov, 1967; Kravtsov and Berczynski, 2004; Kravtsov *et al.*, 1999; Kravtsov and Orlov, 1983; Kravtsov and Zhu, 2010). Note all these methods describe caustics associated diffraction. However, the deep shadow zone can be also insonified by scattering due to turbulence (Ostashev and Wilson, 2015) or more likely at low frequencies by fine structures of the middle and upper atmosphere (Kulichkov *et al.*, 2002, 2010).

Kravtsov was the first one to detail numerical implementation of complex ray theory (Egorchenkov and Kravtsov, 2001). Chapman *et al.* (1999) applied this theory to various types of caustics. Complex rays were also applied for seismic propagation for viscoelastic media (Thomson, 1997; Wu *et al.*, 2021). Finally, complex rays have recently been applied in aeroacoustics to predict high frequency acoustic propagation in subsonic mean jet flow (Stone *et al.*, 2018). This last study is the first one to investigate complex ray tracing in a moving medium.

Large sound speed stratifications, wave advection by wind, multiple arrivals due to stratospheric and thermospheric waveguides and impulsive sources are key features of infrasound propagation. Key features of infrasound propagation involve: 1) sound speed stratification between around 340 m/s at the ground, 280 m/s at the tropopause, 330 m/s at the stratopause and 400 m/s or more in the thermosphere, 2) wave advection by wind with tropospheric jets of the order of 30 m/s and stratospheric ones of the order of 50 m/s undergoing seasonal inversions, 3) and consequently multiple arrivals depending on the direction and intensity of these jets. An example is found in Fig. 1 with a stratospheric wind inducing both stratospheric and thermospheric arrivals. In this configuration, a classical shadow zone exist at ground level up to more than 200 km introduced by the upward refraction in the troposphere. Moreover, infrasound are generally emitted as impulsive signals from transient sources (explosions, volcanoes, meteorites, lightning) with the noticeable exception of swell.

The main objective of our work is to propose an adapted algorithm to predict efficiently by complex ray theory characteristics of infrasonic signals at ground level: arrival times, apparent velocities, azimuths, amplitudes and pressure waveforms. In particular, we emphasize the development of a specific algorithm searching for complex eigenrays between the source and the receiver.

Firstly, in section II, we recall the complex ray theory including equations of both ray tracing and pressure amplitude. In section III we introduce the realistic case of a ground-based point source (explosion source) in a stratified atmosphere with a shear wind jet. In the next section IV, the numerical algorithm searching for eigenrays is detailed, with this case as an example. Physical results are presented in section V and compared to simulations based on a parabolic approximation.

Such a comparison is also performed in the case of a range dependent atmospheric profile in section VI. We summarize our work in section VII and give some perspectives for improvement.

II. COMPLEX GEOMETRICAL ACOUSTICS

Geometrical acoustics, i.e. ray theory, is a standard way to compute infrasound propagation (Pierce, 1994). Ray theory requires acoustic wavelengths to be small compared with atmospheric scales. It conveys the idea that the wavefront motion is mostly due to a combination of acoustic propagation and convection by wind. In subsections II A and II B, we define equations of ray paths and amplitude along rays. All equations and parameters are here written in a two dimensional space (x, z) but can potentially be generalized in three dimensions.

A. Ray tracing

The propagation of impulsive infrasound waves in a windy inhomogeneous atmosphere can be described by linear geometrical acoustics. The underlying assumptions are that the acoustic perturbation is located near a wavefront and that medium properties vary slowly over a typical wavelength. The wavefront, defined implicitly by $\Phi(\boldsymbol{x}, t) = 0$, evolves spatially with the time t following the eikonal equation:

$$\left(\frac{\partial \Phi}{\partial t} + \boldsymbol{v} \cdot \boldsymbol{\nabla} \Phi\right)^2 = c^2 \boldsymbol{\nabla} \Phi \cdot \boldsymbol{\nabla} \Phi, \tag{1}$$

with c the sound speed and $\boldsymbol{v}$ the wind velocity. This equation is derived from linearized Euler equations using either a multiple-scale asymptotic analyzis (Gréa *et al.*, 2005; Pierce, 1994; Scott *et al.*, 2017; Stone *et al.*, 2018) or by applying the WKB ansatz to the Helmholtz equation (Babich and Buldyrev, 1991; Candel, 1977; Chapman *et al.*, 1999; Kravtsov, 1967; Thomson, 1997). The eikonal equation has two roots, which implies a choice of sign associated with the direction of propagation of the wavefront along $\boldsymbol{\nabla}\Phi$ so that:

$$\frac{\partial \Phi}{\partial t} + \boldsymbol{w} \cdot \boldsymbol{\nabla}\Phi = 0, \tag{2}$$

with $\boldsymbol{w} = c\boldsymbol{n} + \boldsymbol{v}$ the group velocity and $\boldsymbol{n} = \boldsymbol{\nabla}\Phi/\sqrt{\boldsymbol{\nabla}\Phi \cdot \boldsymbol{\nabla}\Phi}$ the unit normal ($\boldsymbol{n} \cdot \boldsymbol{n} = 1$) to the surface $\Phi =$ constant at constant time. This eikonal equation (Eq. (2)) implies that the wavefront surface $\Phi =$ constant moves with velocity $\boldsymbol{w}$. Here, both real and complex solutions of the eikonal equation (Eq. (2)) are considered. Real solutions are associated with classical geometrical acoustics in the illuminated (insonified) zone, while complex solutions are associated with diffracted waves into shadow (silent) zones. For complex solutions, Φ, $\boldsymbol{x}$ and t are complex-valued. The sound speed $c(\boldsymbol{x}, t)$ and wind vector $\boldsymbol{v}(\boldsymbol{x}, t)$ are extended as holomorphic functions in the complex plane (Chapman *et al.*, 1999; Kravtsov, 1967; Thomson, 1997). In the eikonal equations (1) and (2), the scalar product of complex vectors is the Euclidean one, $\boldsymbol{a} \cdot \boldsymbol{b} = \sum_k a_k b_k$ with a_k and b_k real or complex quantities (Kravtsov, 1967). For complex vectors, this scalar product is neither real nor zero-definite, but is a holomorphic function.

Rays are the characteristic curves of the eikonal Eq. (2) (Courant and Hilbert, 2008). $\Phi(\boldsymbol{X}, t)$ is constant along a given ray $\boldsymbol{X}$ whose position evolves according to the ray-tracing equation

$$\frac{\mathrm{d}\boldsymbol{X}}{\mathrm{d}t_a} = c\boldsymbol{n} + \boldsymbol{v}. \tag{3}$$

Here t_a, the wave travel time along the ray, is considered as an integration parameter. Note that the ray integration parameter could also be the physical ray length. However, t_a is the natural integration parameter for a time dependant media. Taking the gradient of (2) and setting $\boldsymbol{K} = \boldsymbol{\nabla}\Phi$ along rays give

$$\frac{\mathrm{d}\boldsymbol{K}}{\mathrm{d}t_a} = -K\boldsymbol{\nabla}c - \boldsymbol{\nabla}\boldsymbol{v}\cdot\boldsymbol{K}. \tag{4}$$

The two rays equations (3) and (4) form a closed system with $\boldsymbol{n} = \boldsymbol{K}/K$ and $K = +\sqrt{\boldsymbol{K}\cdot\boldsymbol{K}}$. The positive sign determines the direction of propagation according to the sign chosen for (2). This system of ray equations is valid for a three dimensional, inhomogeneous, time dependent and convected atmosphere. With the underlying assumptions of ray theory, the wavefront $\Phi(\boldsymbol{x}, t) = 0$ is considered as locally plane with local wave pulsation $\omega = -\partial\Phi/\partial t$ and local wavevector $\boldsymbol{K} = \boldsymbol{\nabla}\Phi$. The eikonal Eq. (2) is locally equivalent to the dispersion relation $\omega = \boldsymbol{K}\cdot\boldsymbol{w}$. For a time independent media, ω is constant along rays (Candel, 1977). In this case, the equations can be written in a Hamiltonian form (Gréa *et al.*, 2005; Lalande *et al.*, 2012; Thomson, 1997; Virieux *et al.*, 2004) and Φ is related to the wave phase.

The wavefront at the source is defined as $\Phi(\boldsymbol{x}_s, t_s) = 0$ with $\boldsymbol{x}_s$ the source position and t_s the time at the source. Initial conditions for rays at the source also involve the wavefront unit normal $\boldsymbol{n}_s$ at the source:

$$\boldsymbol{X}(\phi, t_s) = \boldsymbol{x}_s, \quad \boldsymbol{K}(\phi, t_s) = k_s\boldsymbol{n}_s, \tag{5}$$

with $k_s = \omega/(c(\boldsymbol{x}_s, t_s) + \boldsymbol{n}_s \cdot \boldsymbol{v}(\boldsymbol{x}_s, t_s))$. For two dimensional propagation, only one parameter ϕ defines the initial conditions, e.g. the geometrical shape of the initial wavefront (a curved line). This parameter is specific to the investigated source. Two parameters are needed at 3D, as the initial wavefront is then a curved surface.

For a 2D point source modeling an explosion, ϕ is the ray elevation angle so that $\boldsymbol{n}_s = \cos\phi \boldsymbol{e}_x + \sin\phi \boldsymbol{e}_z$, with $(\boldsymbol{e}_x, \boldsymbol{e}_z)$ the unit vectors in the horizontal x and vertical z directions respectively. The source position $\boldsymbol{x}_s$ and the time at the source t_s are independent of ϕ. For a 3D point source modeling an explosion, we add another emission parameter corresponding to the emission azimuth ψ. In that case $\boldsymbol{n}_s = \cos\phi \sin\psi \boldsymbol{e}_x + \cos\phi \cos\psi \boldsymbol{e}_y + \sin\phi \boldsymbol{e}_z$, with $\boldsymbol{e}_y$ the unit vector in the y direction.

Ray equations (3) and (4) with initial conditions (5) are solved for all values of the ray parameter ϕ to obtain the full set of rays $\boldsymbol{X}(\phi, t_a)$, $\boldsymbol{K}(\phi, t_a)$. For complex rays, these equations and initial conditions remain the same, with all parameters now getting complex-valued in the 4D complex space.

In a two dimensional complex space $\boldsymbol{x} = (x, z)$, the associated manifold is of dimension 4. Complex rays are hyperplanes (of dimension 2) of the complex space described by $\boldsymbol{X}(\phi, t_a)|_\phi$ where t_a is a complex-valued. Complex wavefronts $\Phi(\boldsymbol{x}, t) = 0$ at a given time t_a are two dimensional hypersurfaces defined by $\boldsymbol{X}(\phi, t_a)|_{t_a} = \text{constant}$. Nevertheless, only real points $\boldsymbol{X}(\phi, t_a)$ are physical solutions (Kravtsov, 1967; Thomson, 1997). For complex rays, generally only one position of the two dimensional manifold is real, compared to real rays where every point is real. The main difficulty of complex ray tracing is therefore to ensure that the ray point physically representing the receiver $\boldsymbol{x}_r$, is real. The determination of ray parameters (ϕ, t) associated with real receivers, is a two point boundary value problem (Press *et al.*, 1996; Stone *et al.*, 2018). This problem is solved numerically in section IV. Furthermore, complex ray solutions at a real receiver in the shadow zone are complex conjugates. Only one is physical, the one keeping the amplitude of the solution bounded at large distances in the shadow zone (Egorchenkov and Kravtsov, 2001; Kravtsov and Orlov, 1983).

B. Field amplitude

To compute the evolution of the wave amplitude along rays, the asymptotic expansion of linearized Euler equation leads at second order to the transport equation (conservation of wave action) (Blokhintzev, 1946; Gréa *et al.*, 2005; Pierce, 1994; Scott *et al.*, 2017; Stone *et al.*, 2018). This one can also be obtained from the Helmholtz equation (Babich and Buldyrev, 1991; Candel, 1977; Chapman *et al.*, 1999; Kravtsov, 1967; Thomson, 1997).

$$\frac{\partial A}{\partial t} + \boldsymbol{\nabla} \cdot (\boldsymbol{w}\mathrm{A}) = 0, \tag{6}$$

with $\boldsymbol{w} = c\boldsymbol{n} + \boldsymbol{v}$ the group velocity and $A = p^2/K\rho c^3$ the wave action with p the acoustic overpressure and ρ the atmospheric density. For time independent media this conservation equation is reduced to $\boldsymbol{\nabla} \cdot (\boldsymbol{w}\mathrm{A}) = 0$ (Candel, 1977).

At a position $\boldsymbol{X}(t_a)$ along one given ray, the acoustic overpressure signature $p(\boldsymbol{X}, t)$ is approximated by (Scott *et al.*, 2017):

$$p(\boldsymbol{X}(t_a), t) = K \left(\frac{\rho c^3}{\nu}\right)^{1/2} u(\Phi(\boldsymbol{X}(t_a), t), t_a), \tag{7}$$

where the wavenumber K and the infinitesimal ray tube area ν are evaluated along the ray at t_a, atmospheric sound speed c and atmospheric density ρ are evaluated at $\boldsymbol{X}(t_a)$. At two dimensions, $\nu = (\boldsymbol{X}_\phi \wedge \boldsymbol{e}_y) \cdot \boldsymbol{n}$ in the (x, z)-plane. The ray tube area ν is computed using geodesic equations described in (Scott *et al.*, 2017, Eq. A1 and A2) or in (Blom and Waxler, 2017, Eq. 5 and 6) where they are called equations of auxiliary parameters. Here these equations keep unchanged but get fully complex considering the correct definition for complex-valued K. For linear propagation in a non-absorbing media, the normalized waveform $u(\xi, t_a)$ is conservative along rays:

$$\frac{\mathrm{d}u}{\mathrm{d}t_a} = 0, \tag{8}$$

where $\xi = \Phi(\boldsymbol{x}, t_a)$ is the scaled distance to the wavefront and is zero on the wavefront.

In the wavefront vicinity $\Phi(\boldsymbol{X}(t_a), t_a) = 0$, a Taylor expansion leads to $\xi = \Phi(\boldsymbol{X}(t_a), t) \approx \omega(t_a - t)$ where $\omega = \boldsymbol{K} \cdot \boldsymbol{w}$. For complex rays reaching a receiver at $\boldsymbol{X}(t_a)$ located in shadow zones with a complex-valued t_a, $\mathrm{Re}(\xi) = \mathrm{Re}(\omega(t_a - t))$ and $\mathrm{Im}(\xi) = \mathrm{Im}(\omega t_a)$ at a time t close to t_a. This closed-form approximation of ξ is replaced in (7).

Because the ray tube area $\nu(t_a)$ may vanish at the source t_s, the conservation of wave action along a given ray has to be initialized slightly away from it, at actual emission time t_e. For each ray, the scaled waveform $u(\xi, t_e)$ and the ray cross section ν_e are defined at this emission time t_e, sufficiently close to the source so that we can assume propagation in a homogeneous medium during the small time interval $t_e - t_s$. There the ray tube area is not zero anymore, $p(\boldsymbol{X}(t_e), t)$ is assumed to be known and real, and is used to quantify the pressure field all along the ray.

We extend $u(\xi)$ for complex values of the phase function ξ by means of the Fourier transform:

$$u(\xi) = \frac{1}{2\pi}\int_{-\infty}^{\infty} \tilde{u}(q)\mathrm{e}^{-|q|\mathrm{Im}(\xi)}\mathrm{e}^{iq\mathrm{Re}(\xi)}\mathrm{d}q, \tag{9}$$

where function $\tilde{u}(q)$ is obtained from the real function $u(\xi)$

$$\tilde{u}(q) = \int_{-\infty}^{\infty} u(\xi)\mathrm{e}^{-iq\xi}\mathrm{d}\xi. \tag{10}$$

We can note that $q\omega/2\pi$ is the physical frequency and $|\boldsymbol{K}|q$ the physical acoustic wavenumber. To preserve the asymptotic decay of the amplitude (Chapman, 2004) into shadow zone when $q < 0$, the complex conjugate of all parameters $(t, \xi, \phi, \boldsymbol{X}, \boldsymbol{K}, \nu)$ should be taken. If ξ is real-valued, i.e. for real rays, we find the classical real Fourier transform of $\tilde{u}(q)$.

The Hermitian symmetry of the argument $\tilde{u}(q)\mathrm{e}^{-|q|\mathrm{Im}(\xi)}$ shows that the waveform $u(\xi)$ remains a real-valued signature. For a time independent media (ω is constant), in the shadow zone, we find the classical behavior of the argument $\mathrm{e}^{-|q\omega|\mathrm{Im}(t_a)}$ imposing $\mathrm{Im}(t_a) > 0$ along rays, with an exponential decay proportional to the physical frequency $q\omega/2\pi$ (Chapman *et al.*, 1999; Kravtsov, 1967).

For both real and complex rays, the quantity $\sqrt{\nu}$ in Eq. (7) should be analyzed. Along real rays, a caustic is encountered when $\nu = 0$, leading to an infinite amplitude (Jensen *et al.*, 1995; Pierce, 1994) and a change of sign for ν. Using complex notation $\nu = |\nu|\mathrm{e}^{i\theta}$, $\theta = \arg(\nu)$ undergoes a π increase each time a caustic is encountered. It is therefore convenient to introduce the number n_c (Chapman, 2004; Jensen *et al.*, 1995) of caustics crossed along a ray starting from the source, so that $\theta - \theta_e = \mathrm{n}_c\pi$, with $\theta_e = \arg(\nu_e)$. Note that for real rays with $\nu_e < 0$, $\theta_e = \pm\pi$.

For real rays, the square root in (7) is rewritten as $\sqrt{\nu} = |\nu|^{1/2} \mathrm{e}^{i(\mathrm{n}_c\pi/2+\theta_e/2)}$. Using these complex notations, we obtained for real rays the $\pi/2$ signal phase shift at caustic of the catastrophe theory (Chapman, 2004; Kravtsov and Orlov, 1983; Thom, 1983). We can note that the argument of $\sqrt{\nu}$ is 2π periodic and that θ should be considered at least 4π periodic. It should be noted that the choice of the sign of θ is made with the choice of the pulsation q sign with respect to Fourier transform convention (10). Therefore, the acoustic overpressure for each ray is obtained by taking the real part of p:

$$\begin{aligned} p(\boldsymbol{X}(t_a), t) = \frac{1}{2\pi} \int_{-\infty}^{\infty} K \left(\frac{\rho c^3}{|\nu|}\right)^{1/2} \tilde{u}(q) \\ \times \exp\left[-i\mathrm{sgn}(q)\theta/2 - |q|\mathrm{Im}(\omega t_a) + iq\mathrm{Re}(\omega(t_a - t))\right] \mathrm{d}q. \end{aligned} \tag{11}$$

Assuming linear acoustics in the caustic region, shows that for one ray, the waveform after crossing a caustic is the Hilbert transform of the waveform before crossing the caustic. Then, in the Fourier domain, for a waveform leaving the caustic $\tilde{u}_{\mathrm{out}}(q)$ and an arriving waveform $\tilde{u}_{\mathrm{in}}(q)$: $\tilde{u}_{\mathrm{out}}(q) = -i\mathrm{sgn}(q)\tilde{u}_{\mathrm{in}}(q)$, for real rays.

Finally, if several rays arrive at a given receiver, all their contributions have to be added. We can have both real and complex rays at the same receiver, for example close to a cusp caustic.

For time independent media, ω is real and constant, then, in the frequency domain, ωq is substituted by the physical pulsation $\tilde{\omega}$ in Eq. (11). The overall overpressure at the receiver point $\boldsymbol{x}$ of all eigenrays subfixed by j is:

$$\begin{aligned} \tilde{p}(\boldsymbol{x}, \tilde{\omega}) = \sum_j K \left(\frac{\rho c^3}{|\nu_j|}\right)^{1/2} \tilde{u}\left(\frac{\tilde{\omega}}{\omega}\right) \\ \times \exp\left[-i\mathrm{sgn}(\tilde{\omega})\theta_j/2 - |\tilde{\omega}|\mathrm{Im}(t_{aj}) + i\tilde{\omega}\mathrm{Re}(t_{aj} - t)\right]. \end{aligned} \tag{12}$$

To study the neighborhood of the caustic ($\nu \to 0$), the method of complex rays can be completed with for example Maslov's method (Kravtsov and Zhu, 2010) which is not treated in this paper, or the uniform asymptotic theory at the caustic.

C. Uniform theory of diffraction at the caustic

Uniform theory of diffraction (UTD) provides an accurate value of the overpressure amplitude in the neighborhood of the caustic singularity, uniformly dependent on the frequency, and which matches asymptotically geometrical complex ray theory (White and Pedersen, 1981). In the insonified zone of a fold caustic, two rays arrive respectively at time t_{fast} for the fast direct ray, and at time t_{slow} for the slow ray (which reaches the considered point $\boldsymbol{x}_c$ after having tangented the caustic). Therefore one has $\boldsymbol{X}(t_{\text{fast}}) = \boldsymbol{X}(t_{\text{slow}}) = \boldsymbol{x}_c$. This pair arrivals are discussed in detail for stratospheric ones by Waxler *et al.* (2015), see especially their figures 9 and 10. The interference and diffraction of the two rays is mainly characterized by the scaled time difference $\tau = \frac{\omega_{\text{slow}}+\omega_{\text{fast}}}{4}(t_{\text{slow}} - t_{\text{fast}})$ which is a positive value. Following White and Pedersen (1981), the overpressure signature of the uniform theory in the insonified zone is defined using Airy's function Ai and its derivative Ai$'$ as

$$\begin{aligned}
p_c(\boldsymbol{x}_c, t) = \frac{1}{2\pi}\int_{-\infty}^{\infty} \Bigg[& \left(\frac{U_{\text{slow}}}{|\nu_{\text{slow}}|^{\frac{1}{2}}} + \frac{U_{\text{fast}}}{|\nu_{\text{fast}}|^{\frac{1}{2}}}\right)\pi^{\frac{1}{2}}(-\zeta)^{\frac{1}{4}}\mathrm{Ai}(\zeta) \\
& + i\,\mathrm{sgn}(q)\left(\frac{U_{\text{slow}}}{|\nu_{\text{slow}}|^{\frac{1}{2}}} - \frac{U_{\text{fast}}}{|\nu_{\text{fast}}|^{\frac{1}{2}}}\right)\pi^{\frac{1}{2}}(-\zeta)^{-\frac{1}{4}}\mathrm{Ai}'(\zeta)\Bigg] \\
& \times \exp\Bigg[-i\,\mathrm{sgn}(q)\left(\frac{\theta_{\text{slow}}+\theta_{\text{fast}}}{4}\right) \\
& + iq\left(\frac{\omega_{\text{fast}}t_f + \omega_{\text{slow}}t_s}{2} - \frac{\omega_{\text{fast}}+\omega_{\text{slow}}}{2}t\right)\Bigg]\,\mathrm{d}q,
\end{aligned} \tag{13}$$

with $\zeta = -(\frac{3}{2}|q|\tau)^{2/3}$ and the amplitudes $U_i(q) = K_i \tilde{u}_i(q)(\rho_i c_i^3)^{1/2}$ with $i =$ slow or fast. Far from the caustic, when $\zeta \to -\infty$, Eq. (13) matches perfectly with the sum of geometrical ray theory overpressures (11) $p(\boldsymbol{X}(t_{\text{fast}}), t) + p(\boldsymbol{X}(t_{\text{slow}}), t)$. In the shadow zone, the overpressure signature of the uniform theory is defined from the single complex ray at position $\boldsymbol{X}(t_d)$ as

$$
\begin{aligned}
p_c(\boldsymbol{X}(t_d), t) = \frac{1}{2\pi} \int_{-\infty}^{\infty} \frac{2U_d}{|\nu_d|^{\frac{1}{2}}} \pi^{\frac{1}{2}} \Bigg[&\cos\left(\frac{\theta_d - \theta_{\text{fast}}}{2} - \frac{\pi}{4}\right) \zeta^{\frac{1}{4}} \mathrm{Ai}(\zeta) \\
&+ i\,\mathrm{sgn}(q) \sin\left(\frac{\theta_d - \theta_{\text{fast}}}{2} - \frac{\pi}{4}\right) \zeta^{\frac{1}{4}} \mathrm{Ai}'(\zeta) \Bigg] \\
&\times \exp\left[-i\,\mathrm{sgn}(q) \left(\frac{\theta_{\text{fast}}}{2} + \frac{\pi}{4}\right) + iq\mathrm{Re}\left(\omega_d(t_d - t)\right) \right] \mathrm{d}q,
\end{aligned}
\tag{14}
$$

with $\zeta = \left(\frac{3}{2}|q|\mathrm{Im}(\omega t_d)\right)^{2/3}$ and the amplitude $U_d(q)$ of the complex ray. θ_{fast} is the angle of ν for the real incident ray at the caustic and its value is a multiple of π. Up to a medium distance to the caustic, $\theta_{\text{fast}} = \theta_d - (\theta_d[\pi])$, with [] the modulo operator.

Far from the caustic, when $\zeta \to \infty$, Eq. (14) matches perfectly the overpressure (11) of the geometrical complex ray theory. At the caustic, when $\zeta \to 0$, Eq. (13) and Eq. (14) reach the same limit without singularity. Finally, for other rays which arrived at the receiver and are not connected with the caustic, their contribution sum independently as in Eq. (12).

D. Numerical complex ray integration

Rays equations (3) and (4) and geodesic equations constitute an inhomogeneous system of complex ordinary differential equations depending on the complex variable t_a:

$$
\frac{\mathrm{d}\boldsymbol{F}}{\mathrm{d}t_a} = \boldsymbol{R}(\boldsymbol{F}, t_a), \tag{15}
$$

with $\boldsymbol{R}(\boldsymbol{F})$ a function of the eight-dimensional complex vector $\boldsymbol{F}$ (twelve dimensions at 3D) with a known initial condition at the source $\boldsymbol{F}(t_s)$. This system is integrated between the complex emission time t_s and the complex final time t_a following any path $t_\sigma(\sigma)$ in the complex plane, with σ a real curvilinear variable such that $t_\sigma(0) = t_s$ and $t_\sigma(1) = t_a$, (Hille, 1997). The complex system of differential equations can therefore be recast as depending on real variables :

$$\frac{\mathrm{d}\boldsymbol{F}(t_\sigma(\sigma))}{\mathrm{d}\sigma} = \frac{\mathrm{d}t_\sigma}{\mathrm{d}\sigma}\boldsymbol{R}(\boldsymbol{F}, t_\sigma(\sigma)). \tag{16}$$

and evaluated numerically using a classical Runge and Kutta 4^{th} order scheme (Press *et al.*, 1996). In this paper, as in Amodei *et al.* (2006); Egorchenkov and Kravtsov (2001); Kravtsov and Zhu (2010); Thomson (1997), a straight integration path is always used with $t_\sigma(\sigma) = t_s + \sigma(t_a - t_s)$ and $\mathrm{d}t_\sigma/\mathrm{d}\sigma = (t_a - t_s)$ which is indentified for the sake of simplicity with the *complex ray*. Other paths could be considered to overlap singularities of the atmospheric profiles, but are not considered here.

As only real points $\boldsymbol{X}(\phi, t)$ are physical solutions (Kravtsov, 1967; Thomson, 1997), a numerical method is used to find eigenrays at receivers $\boldsymbol{x}$ such that $\boldsymbol{X}(\phi, t) = \boldsymbol{x}$. For complex rays, four parameters ($\mathrm{Re}(\phi)$, $\mathrm{Im}(\phi)$, $\mathrm{Re}(t_a)$, $\mathrm{Im}(t_a)$) must be optimized. The numerical method is detailed using a realistic case in the section IV.

III. POINT SOURCE IN A WINDY ATMOSPHERE

We consider an impulsive point source on the ground, at the position $\boldsymbol{x}_s = (0, 0)$ and with the emission time at the source $t_s = 0$. The initial spherical wavefront is defined by its normal vector $\boldsymbol{n}_s = \cos\phi\boldsymbol{e}_x + \sin\phi\boldsymbol{e}_z$, with ϕ the emission angle. Infrasound generated by this source can propagate at long range due to the thermospheric and the stratospheric waveguides (Blom, 2019; Drob *et al.*, 2003; Scott *et al.*, 2017). The thermospheric waveguide is associated with the increase in the thermosphere of the atmospheric temperature vertical profile. To model this one, we use the realistic profile defined by rational function (Lingevitch *et al.*, 1999, Eq. (49)). The associated sound speed profile c presented in Fig. 1(a) satisfies the analytical condition of the complex ray method. The stratospheric waveguide is associated with combined effects of the increase of the both temperature in the stratosphere and the stratospheric wind jet. For the wind, we use an analytical Gaussian profile (Blom, 2019):

$$\boldsymbol{v} = v_w \ \mathrm{e}^{-\frac{(z-z_w)^2}{\sigma_w^2}} \boldsymbol{e}_x, \tag{17}$$

with a maximum jet speed $v_w = 50\,\mathrm{m/s}$ observed at an altitude $z_w = 60\,\mathrm{km}$ and with a width of the Gaussian distribution $\sigma_w = 17.5\,\mathrm{km}$. The effective sound speed in $\boldsymbol{e}_x$ direction $c_{\mathrm{eff}} = c+v$ is shown in Fig. 1(a). The ray computation is performed with these expressions of c and $\boldsymbol{v}$ through equations (3) and (4). Resulting real rays, obtained with the shooting method with ϕ variation between 0 and 60 degrees with $\Delta\phi = 0.5°$, are represented in Fig. 1(b). For the sake of clarity the reflected rays are not represented. This advected profile gives stratospheric and thermospheric arrivals. Each kind of arrivals have direct rays (black) and that which crossed a caustic (gray). The stratospheric and thermospheric caustics (purple dashed thick lines) are both altitude cusp caustics whose one branch continues until the ground. These caustics begins at $x = 133\,\mathrm{km}$ with an altitude of $45\,\mathrm{km}$ for the stratospheric one and at $x = 214.2\,\mathrm{km}$ with an altitude of $123\,\mathrm{km}$ for the thermospheric one. At ground level, rays focusing form two locally fold caustics and thus, two shadow zones. The stratospheric ground caustic is located at $x = 225.7\,\mathrm{km}$ and the thermospheric one at $x = 361.8\,\mathrm{km}$. The ray intersection with the ground, necessary to be known for the complex ray method, is indicated with black and gray dots in Fig. 1(b)

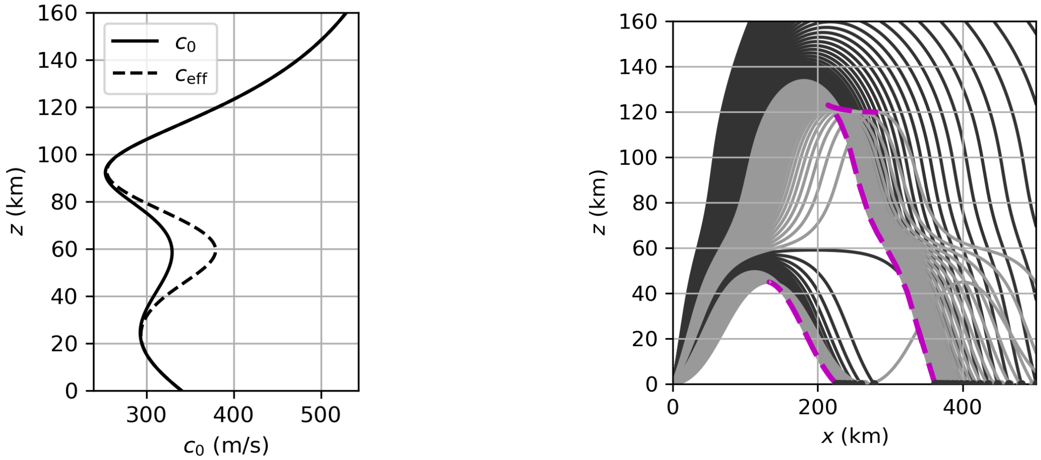

(a) (b)

Fig. 1. (a) Rational sound speed profile c (solid line) of (Lingevitch *et al.*, 1999) and effective sound speed profile $c_{\text{eff}} = c + v$ (dashed line) with Gaussian wind profile (Blom, 2019). (b) Real rays obtained with ray shooting method, for an emission angle varying from 0 to 60 degrees. Stratospheric and thermospheric caustics are indicated by purple (color inline) dashed thick lines. Gray rays reach the ground after having through one caustic.

IV. EIGENRAYS ALGORITHM

In this section, we consider receivers at ground level between 1 and 500 km from the source. We present the numerical process of integration and optimization, to obtain real and complex eigenrays.

Numerically, a difficulty of the complex ray tracing method is the determination of all eigenrays at a given receiver $\boldsymbol{x}_r$. Searching for eigenrays means computing all couples of complex ray parameters $(\phi,\, t)$ satisfying $\boldsymbol{X}(\phi, t) = \boldsymbol{x}_r$ for the real receiver position $\boldsymbol{x}_r$. As exemplified below, multiple eigenrays can reach a single receiver. This multi-valued problem can be recast as a classical two points boundary value problem (Press *et al.*, 1996; Stone *et al.*, 2018) with, in the general complex case, four real unknowns : $\mathrm{Re}(\phi)$, $\mathrm{Im}(\phi)$, $\mathrm{Re}(t)$ and $\mathrm{Im}(t)$. Four parameters generate a too large space to be numerically explored at reasonable costs to find all eigenray solutions. Additionally, some complex numerical solutions can be unphysical. Therefore, we restrict the problem to complex eigenrays connected to real rays through a caustic. This allows one to use a real ray tracing method to identify real eigenrays, and then to extend the solution to shadow zones. This strategy gives a numerically tractable way to find all physical eigenrays at receivers. However, it is necessary to identify all caustics, bounds of waveguides and ground limited rays for the real ray tracing problem. Moreover, caustics are singularities where the Jacobian determinant of the transformation from ray parameters (ϕ, t) to spatial coordinates $\boldsymbol{x}$ vanishes. This singularity is a numerical difficulty for optimization algorithms, especially in the vicinity of the caustic.

To solve the eigenray problem, we developed an algorithm using real interpolation and extrapolation for real solutions, and complex extrapolation at caustics for complex solutions in the shadow zones. It is illustrated by the previous example of a ground-based point source in a vertically stratified atmosphere with Gaussian wind profile (see Fig. 1(a)). We restrict the problem to ground based receivers with x_r between 1 and 500 km. The process in three steps is described below and illustrated in Fig. 2.

The first step of our method is a *real ray shooting*, with a regularly discretized emission parameter, here the angle ϕ varying from 0 to 60° (see the first line of Fig. 2). The number of integrated rays in this shooting phase is chosen equal to 120. This ϕ democratization is enough to distinguish stratospheric and thermospheric waveguides, as well as caustics. As all receivers are on the ground, we extract all rays intersection with the ground. Then, we obtain one discrete ground position x_i for each launched real ray ϕ_i and the eigenray procedure leads to know all real $\phi(x)$. Ground arrivals form two discrete sets: stratospheric arrivals for ϕ between 0 and 0.45 rad and thermospheric arrivals for ϕ between 0.48 and 0.87 rad. For larger values of ϕ, rays reaching the ground beyond 500 km are not calculated. These two sets have two visible branches of ϕ and t, the direct rays in black and that ones having tangented once a caustic in gray. Caustics and waveguide bounds are both characterized by a sign changes of $\mathrm{d}x/\mathrm{d}\phi$. For caustics $\mathrm{d}x/\mathrm{d}\phi$ goes through zero and for waveguides it jumps from $-\infty$ to $+\infty$ or the inverse (Chapman, 2004, Sec. 2.4). These changes are determined numerically, by searching for changes of sign of quantity $D_i = \frac{x_{i+1}-x_i}{\phi_{i+1}-\phi_i}$. To identify caustics and waveguides, we denote k the point where the sign of D_k changes compared to D_{k-1}, and compare the mean value $(D_{k-1} + D_k)/2$ with the median of the full set of values D_i. If the mean value is lower than the median, we assume that the point is close to a caustic, otherwise that it is close to the limit of a waveguide.

The second step consists in *extrapolating the discrete real ray arrivals to the whole space* (see the second line of Fig. 2). This step will provide, for each ground point, initial guesses for emission parameters of eigenrays, both real and complex. Let us begin with real rays. For receiver positions within the limits of discrete branches obtained in step 1, we simply perform a quadratic interpolation. Resulting points appear in figure as lines with squares with corresponding colors to the shooting step. Boundaries of real discrete branches from step 1, interpreted as a waveguide limit, are real extrapolated with a log fitting (line with circle and same color) so that $x_r = -C \log(|\phi - \phi_w|)$ with $C = c/2$ if $\phi_i \leq \phi_w$ and $C = c$ if $\phi_i > \phi_w$ (Chapman, 2004). The emission parameter associated to the waveguide limit ϕ_w

and the constant c are chosen to minimize the difference between this theoretical function and the computed five values of x_r for the five rays ϕ_{k-3} to ϕ_{k+1}. While in this waveguide configuration x_r is highly sensitive to ϕ_w, the following optimization in step 3 is robust enough so that the finally computed rays indeed reach the receiver with the desired precision.

For complex rays, we use the caustic position referred by index k from step 1. A real interpolation is first performed around the three neighboring points $K = (k-1, k, k+1)$, with a second order polynomial $X_2(\phi)$ with real coefficients, interpolating exactly the three shooting positions x_j at the three emission parameters ϕ_j for $j \in K$. A similar interpolation for arrival time t_a is performed, the resulting polynomial being noted $T_2(\phi)$. Then search for the complex roots of the polynomial $X_2(\phi) - x_r = 0$ provides the complex extrapolation for any receiver x_r in the shadow zone. As the two complex roots are complex conjugate from one another, the selected ϕ solution is such that $\mathrm{Im}(T_2(\phi)) > 0$, so that the pressure field decays exponentially according to Eq. (9). These guesses are indicated as lines with blue upward triangles for the first shadow zone and with red downward triangles in the second one. The penetration range of x_r inside the shadow zones is arbitrarily limited to 120 km. Beyond this range, guess values would be too far from the actual parameters, and optimization process in step 3 would be unsuccessful. This problem will be solved in the next step 3.

The third step (illustrated by the third line of Fig. 2) is the determination of eigenrays by finding the real or complex values (ϕ, t_a) that minimize the quantity $|\boldsymbol{X}(\phi,\, t) - \boldsymbol{x}_r|$. For this we use the *Levenberg-Marquardt* algorithm (LMA) (Moré, 1978; Transtrum and Sethna, 2012), with initial guesses determined in step 2.

LMA is a combination of two minimization methods: gradient descent and Gauss-Newton. For the gradient descent the sum of squared errors is reduced by updating the parameters in the steepest descent direction. For Gauss Newton method, the sum of the squared errors is reduced by assuming that least squares function is locally quadratic and by finding the minimum of this quadratic. Thus, LMA behaves more like gradient descent when parameters are far from the optimum, and more like Gauss Newton when parameters are close. The balance between the two methods is achieved by the damping parameter, that avoids singular Jacobian. In particular, the LMA is efficient in our case around caustic points where the Jacobian vanishes.

For a receiver located deep inside the shadow zone (here in practice at a distance from the caustic larger than 120 km), the initial guess used in the LMA is determined by the output of LMA for the nearest receiver position already computed and closer to the caustic. This implies that eigenrays for receivers in the shadow zone are computed by moving away from the caustic. The distance of 120 km has been chosen as it minimizes the global computation time.

Eigenray solutions are illustrated in Fig. 2 as lines with black and gray dots for real solutions, blue upward triangles for complex solutions in the first shadow zone and red downward triangles for the second shadow zone. The method allows to obtain eigenrays for any receiver position x_r. Here the fifty receivers are shown in Fig. 3 with the corresponding real and complex rays.

Hence, with our complex ray method we are able to obtain all eigenrays for any receiver position x_r with a precision of order 10^{-8} to 10^{-12}.

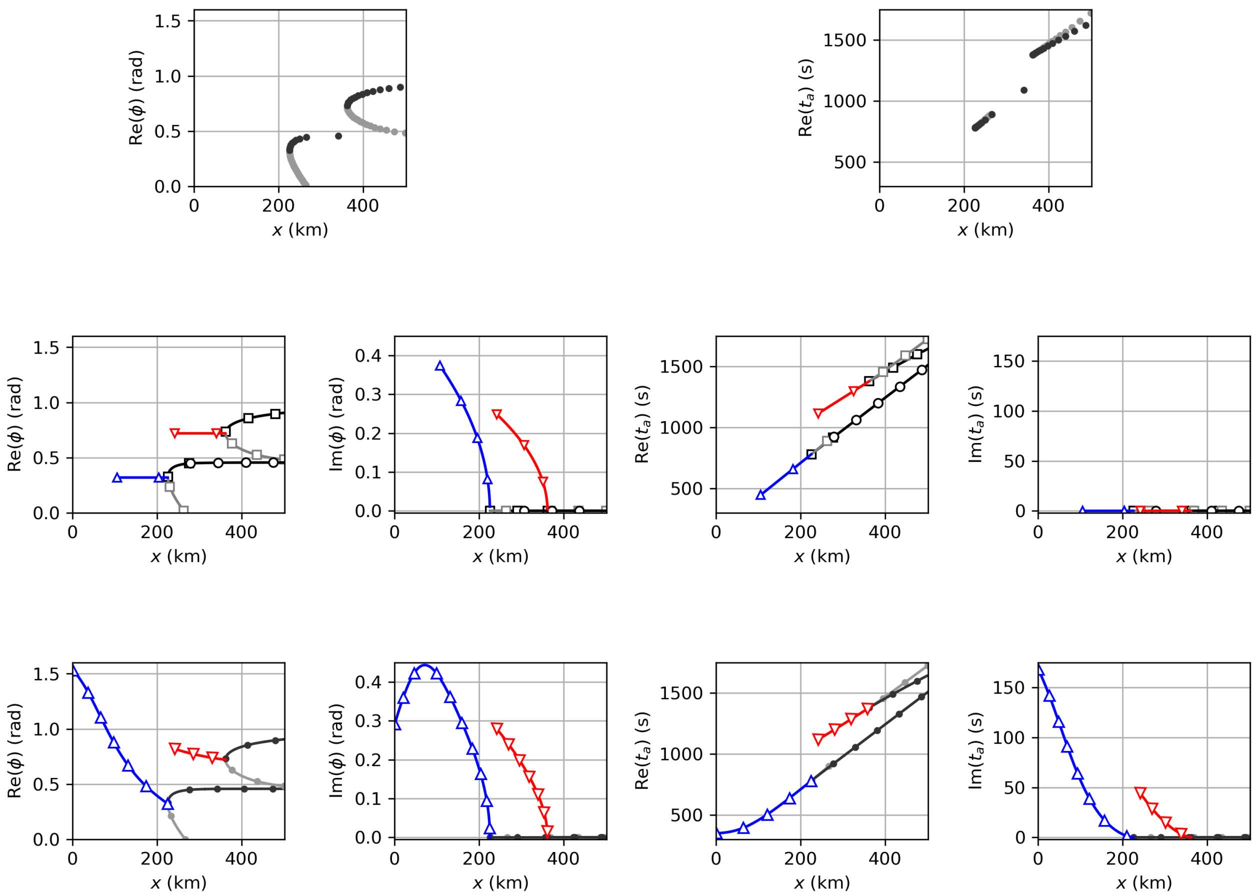

Fig. 2. (color inline) Real and imaginary parts of the emission parameter ϕ and arrival time t. Description of the three-step eigenray research method, on the point source case Fig. 1. First line: ray tracing shooting with the same color code as Fig. 1. Second line: real interpolation (squares), complex extrapolation (triangles - blue upward for stratospheric and red downward for thermorpheric rays) and real extrapolation (circles) of initial guesses. Third line: final eigenrays parameters with the same color code.

V. RESULTS

In this section, we present real and complex eigenrays as well as geometrical parameters for receivers at ground level between 1 and 500 km from the point source. These results are obtained with our complex ray method using the algorithm described in IV and considering the analytical sound speed profile shown in Fig. 1(a).

A. Real and complex ray arrivals at ground level

The optimized emission parameters ϕ and t presented in Fig. 2 and computed with our complex eigenrays algorithm allow to find eigenrays for given receivers. Resulting real and complex rays projected in the real plane (x, z) are represented in Fig. 3(a). Arrivals at ground level due to refraction either in the stratosphere or in the thermosphere are labeled respectively Is and It. For each waveguide (indexed by s for the stratospheric one, and by t for the thermospheric one), there are two arrivals of real rays in insonified zones, the direct or fast one (referred as Is_f and It_f with black points) and the one which tangented a caustic, also called slow arrival (referred as Is_s and It_s with grey points). The presence of these two real rays is clearly visible with the separation of branches for the arrival time and apparent speed (see Fig. 4) with a characteristic cusped wavefront shape. Though these arrivals are always simulated, the time delay between Is_s and Is_f can be quite small. Depending on the frequency f, the two arrivals cannot always be distinguished from one another. The thickness δ of the diffraction boundary layer around the caustic is given by $\delta = (c^2R/2f^2)^{1/3}$ (Buchal and Keller, 1960), where R is the ray curvature relative to the caustic one. At the distance δ, the Airy's function argument ζ used in the UTD equation (13) is equal to $-(2\pi^2)^{1/3}$ and the ray arrival time difference satify $(t_{\mathrm{slow}} - t_{\mathrm{fast}})f = 2\sqrt{2}/3 \approx 0.94$. Following this criteria, the two arrivals can be distinguished at distances from the caustic surface larger than δ, all the larger as the frequency f is larger. For example, for the stratospheric caustic of relative curvature $R = 150\,\mathrm{km}$ and $f = 1\,\mathrm{Hz}$, $\delta \approx 2050\,\mathrm{m}$. These paired arrivals are discussed in details in Waxler *et al.* (2015) and Blom (2019). Even when these two arrivals are theoretically separated, intermediate arrivals due to scattering by fine structures of the atmosphere such as internal gravity waves (Lalande and Waxler, 2016) may obscur this separation especially if one of the two phases is of small amplitude.

At ground level, rays focusing form two fold caustics and thus, two shadow zones. The stratospheric caustic is located at $x = 225.7\,\mathrm{km}$ and the thermospheric one at $x = 361.8\,\mathrm{km}$. In these two shadow zones, field information at any point can be computed with complex rays, shown in Fig. 3 with stratospheric arrivals labeled as $\mathrm{I}s_d$ and thermospheric ones $\mathrm{I}t_d$. We recall that only physical point of complex rays are taken into account and that complex rays are two dimensional surfaces.

To understand the behavior of complex rays, we represent the same rays projected in the plane $(\mathrm{Re}(z), \mathrm{Im}(z))$ and superposed to the colormap of $\mathrm{Im}(c)$ (see Fig. 3(b)). For each real or complex ray, the imaginary part of the altitude $\mathrm{Im}(z)$ is the same for a given real altitude $\mathrm{Re}(z)$. When a complex ray reaches the turning point, also called point of refraction (Chapman, 2004), it goes through the same path in $(\mathrm{Re}(z), \mathrm{Im}(z))$ plane. In other words, the upward and downward paths are symmetric, see Fig. 3(b). Imaginary value of z increases in absolute value as the distance between the real point at the ground

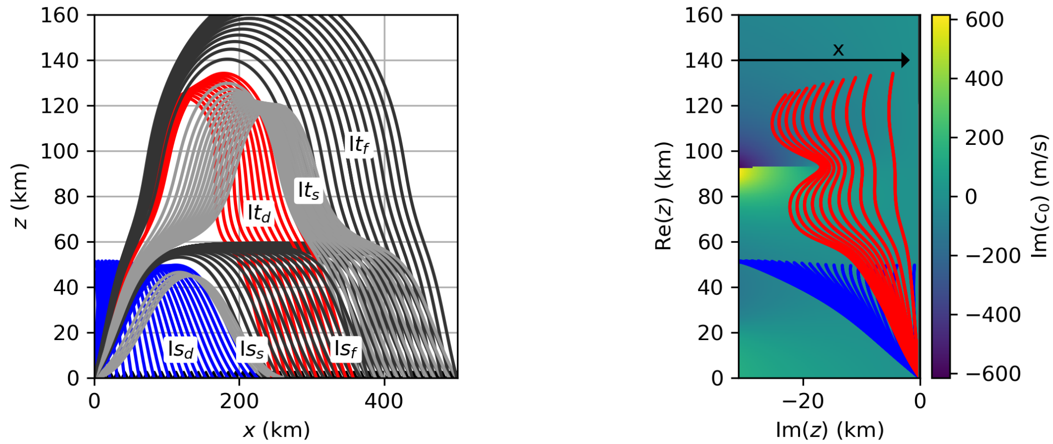

(a) (b)

Fig. 3. (color inline) (a) Eigenrays reaching receivers at the ground obtained with the complex ray tracing method with the same color code as Fig. 2. Real stratospheric ($\mathrm{I}s_s$, $\mathrm{I}s_f$) and thermospheric ($\mathrm{I}t_s$, $\mathrm{I}t_f$) rays, and stratospheric ($\mathrm{I}s_d$) and thermospheric ($\mathrm{I}t_d$) complex rays projected in the real plane (x, z). (b) These same complex rays projected in the $(\mathrm{Re}(z), \mathrm{Im}(z))$ plane with same red/blue color code, superimposed to the colormap of $\mathrm{Im}(c)$. Black arrow indicates increasing x distance of rays ground arrivals.

level and the caustic increases: for instance $\mathrm{Im}(z) = -30\,\mathrm{km}$ (resp. $\mathrm{Im}(z) = -25\,\mathrm{km}$) for the stratospheric (resp. thermospheric) ray nearest to the source. For thermospheric rays, the dip at altitude $\mathrm{Re}(z) = 92\,\mathrm{km}$ corresponds to the minimum of $\mathrm{Re}(c)$. At this position the imaginary part of c changes of sign ($\mathrm{Re}(c_{\mathrm{eff}}) = 0$) which creates a pole preventing the integration of thermospheric complex rays, arriving below $x = 230\,\mathrm{km}$. However, such rays penetrating deep into the shadow zone, would provide a negligible contribution in terms of amplitude. On the contrary, the Gaussian function because it has no singularity, induces no such limitation on ray computation.

B. Geometrical parameters

With a view to compare results with infrasound records at stations, it is interesting to capture frequently used geometrical parameters, such as the arrival time and the horizontal apparent phase velocity $v_a = \omega/k_x$. From ray equations, k_x is constant along rays for a stratified media, and therefore equals its value at the source $v_a = v(z_s) + c(z_s)/\cos\phi$. These quantities are represented for ground receivers in Fig. 4 with same labels and color code as in Fig. 3. As $c(z_s)$ and $v(z_s)$ are constant for a point source, v_a depends only on the emission angle ϕ. Therefore, the evolution of v_a in the shadow zones could not have been found without using the complex ray method which provides $\phi(x_r)$.

For all real arrivals, the apparent velocity v_a is in the range 340 m/s to 550 m/s with lowest values closer to the ground speed of sound of 340 m/s for stratospheric arrivals $\mathrm{I}s_s$ and $\mathrm{I}s_f$, while thermospheric ones reach higher values $\mathrm{I}t_s$ and $\mathrm{I}t_f$ and larger variations. Right at the caustics v_a approximately equals 359 m/s for stratospheric arrival and approximately equals 450 m/s for thermospheric one. For stratospheric complex arrivals $\mathrm{I}s_d$, v_a first increases from 359 m/s at the caustic to 409 m/s at $x = 63$ km and then decreases at higher distance from the caustic where $\mathrm{Re}(\phi) \to \pi/2$. In the second shadow zone $\mathrm{I}t_d$, on the contrary v_a stays roughly constant as $\mathrm{Re}(\phi)$.

Reduced arrival times $t - x/c_{\mathrm{ref}}$ (s) decrease with distance. Indeed, at infinite distance, influence of vertical propagation is negligible, propagation is quasi horizontal and thus reduced time tends to zero. Larger values and larger differences between fast and slow arrivals are observed for thermospheric arrivals, for which vertical stratification effects are more pro-

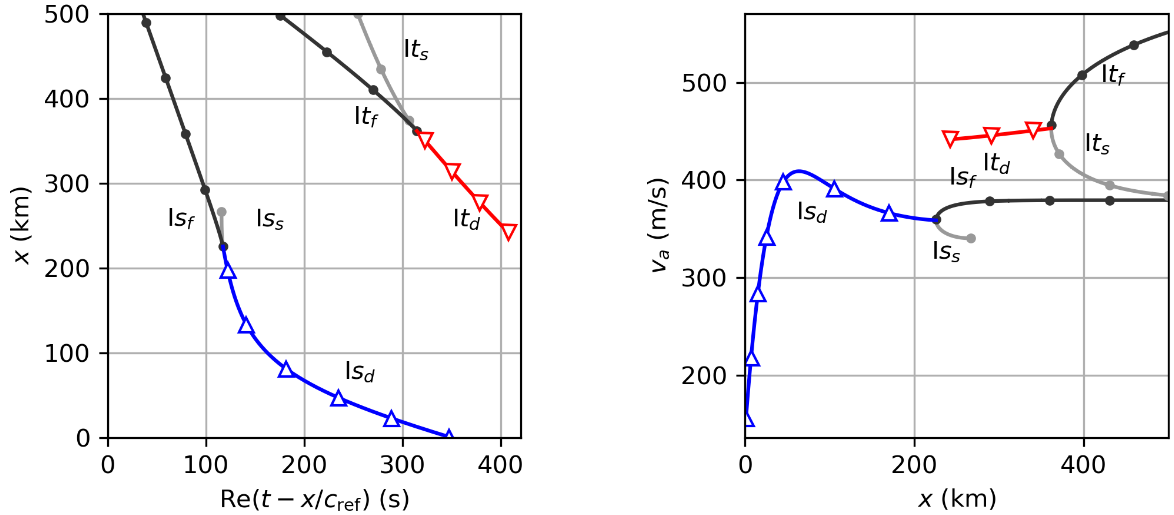

(a) (b)

Fig. 4. (color inline) Real values of geometric parameters at ground receivers. (a) Reduced time $t_{\rm red} = t - x/c_{\rm ref}$ (s) with $c_{\rm ref} = 340\,\mathrm{m/s}$ and (b) apparent velocity v_a (m/s), with same labels and color codes as in Fig. 3.

nounced, than for stratospheric ones. In the shadow zone but close to the caustic, the real value of arrival time of complex rays first tends to linearly extrapolate the limit value at the caustic, as complex rays remove the singularity around caustics. This behavior will be further used to initialize the algorithm searching for eigenrays. Deeper inside the shadow zone, when approaching the source, stratospheric arrivals however deviate more and more from this extrapolation.

C. Comparison of transmission losses with parabolic approximation

Atmospheric infrasound propagation can also be simulated using a two dimensional, fourth order split-step Padé parabolic approximation (Ostashev and Wilson, 2015, p.61), (Collins, 1993; Nguyen-Dinh *et al.*, 2018) with the assumption of effective sound speed (see dashed line Fig. 1(a)). This method accounts for diffraction into shadow zone. However, the effective sound speed assumption may induce some error, in addition to the parabolic approximation. These errors are detailed in (Assink *et al.*, 2017). Nevertheless we use it to validate complex ray tracing method. For a monochromatic point source of frequency $f = 1\,\mathrm{Hz}$ and amplitude p_e, we consider the transmission losses (TL) relatively to $r_{\mathrm{ref}} = 1\,\mathrm{m}$ in dB for ground receivers between 1 and 400 km from the source:

$$\mathrm{TL}(\boldsymbol{x}, \tilde{\omega}) = 20 \log_{10} \left(\frac{|\tilde{p}/p_e|}{\sqrt{r/r_{\mathrm{ref}}}} \right), \tag{18}$$

with $r = x$ the distance to the source and $\tilde{p}$ defined by the Eq. (12) for complex rays. The $\sqrt{r}$ term allows to scale the wave amplitude computed in two dimensions to a three dimensional case with axi-symmetric long range divergence hypothesis. This scaling is also performed in the parabolic approximation solution (Nguyen-Dinh *et al.*, 2018, eq. 5). For a point source at ground level in an homogenous media, $\mathrm{TL} = -20 \log_{10}(r/r_{\mathrm{ref}})$.

Transmission losses obtained with the ray tracing method for each arrival are represented in Fig. 5 independently (with the same color code as in Fig. 3): fast direct real arrivals (black line with dots), slow real arrivals (gray line with dots), complex stratospheric arrivals (blue upward triangles) and complex thermospheric arrivals (red downward triangles). The TL associated with the sum of all rays (green line) and the TL computed with the uniform theory of diffraction of equations (13) and (14) (green dashed lines), are compared to the parabolic approximation TL (black line) for which arrivals can not be distinguished from one another. The propagation allows us to define eight zones between 0 and 400 km, each one associated with a specific physical behavior. Zones I and II are associated with the so called anormal shadow zone (Pierce, 1994), zones III to VI are associated with stratospheric refraction and zones VII and VIII are associated with thermospheric refraction.

Parabolic approximation describes in zone I, which is the closest to the source, the exponential decay of creeping waves (Pierce, 1994) propagating over a rigid ground. This creeping waves contribution is not provided yet by the complex ray method. In zone II, the distance from either the source or the first caustic is such that wave amplitude is indeed exponentially small (-180 dB) so that parabolic approximation reaches the limits of its numerical precision. In insonified zones (IV and VIII), the ray tracing shows the field results from the interference between fast and slow arrivals, either stratospheric ones (Is_f and Is_s) in zone IV and mainly thermospheric ones (It_f and It_s) in zone VIII. Amplitude of the total field oscillates due to these interferences. Ray predicted oscillations are slightly shifted compared to output of the parabolic method, but with similar frequency while amplitudes also show similar levels of transmission losses. The comparison shows that stratospheric and thermospheric ground arrivals are predicted by the parabolic simulation at a shorter distance than by ray tracing. This difference is more important for stratospheric arrivals (1.9 km, see Fig. 6(a)), than for thermospheric ones (1.5 km, see Fig. 6(b)). It is due to the parabolic approximation of the Helmholtz equation, only partly compensated by the use of the effective sound speed c_{eff} (Gainville, 2008). Changing the frequency (we tested 0.1, 0.5, 2 and 5 Hz) does not modify this offset. Such mismatches of the order of the kilometer have been similarly observed in (Assink *et al.*, 2017). Except this position offset, the parabolic equation turns out to be a good reference for an assessment of the complex ray tracing method, especially for the amplitude. As already mentioned, ray-tracing method diverges in a small region around caustics. This singularity of amplitude is resolved using the UTD described in section II C. The solution around caustics is shown with green dashed lines for stratospheric in Fig. 6(a), and thermospheric one in Fig. 6(b). The evolution of the uniform solution allows to reproduce the parabolic solution one and the correct amplitude at the caustic. In the insonified zones (IV and VIII) and except this diffraction layer around caustics, ray tracing and parabolic approximation differ only from 1.2 dB in zone IV, and from 1.3 dB in zone VIII (see Fig. 6). In the main zone of discrepancy (zone V) the geometric field resulting from the interferences of fast and slow stratospheric arrivals $\mathrm{I}s_f$ and $\mathrm{I}s_s$. However, the amplitude of slow ones diverges at the distance of 266.8 km. There, rays emitted at the source at angles approaching zero degree, return to ground after being refracted at an altitude of around 50 km (see gray stratospheric rays $\mathrm{I}s_s$ in Fig. 3(a)). The limit real ray emitted horizontally at the source, tangentially to the ground surface, has a ray tube section which varies along the ray but goes back to zero at the distance of 266.8 km where it tangents the ground for the second time. Hence, the ray method has a singularity in amplitude reduced to one ray (this horizontal ray), again creating an infinite amplification. However, a full caustic does not exist here and cannot be identified as such by our method because it is masked by the ground. This virtual caustic generates diffracted waves at the ground analogous to creeping waves, that are not captured by our complex ray method. Beyond this amplification point (in zone VI), parabolic equation shows the interference of these diffracted waves with geometrical fast stratospheric arrival $\mathrm{I}s_f$, while the ray tracing method gives only the $\mathrm{I}s_f$ contribution, hence a smooth evolution of TL. Transmission Losses are nevertheless of similar orders of magnitude. Inside zones III and

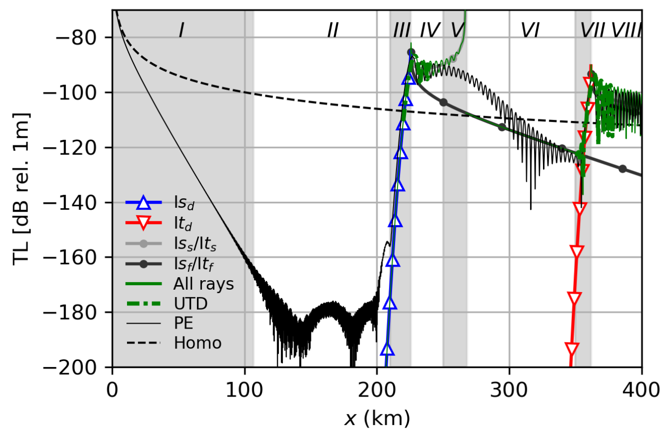

Fig. 5. (color inline) Transmission losses at ground level for a 1 Hz point source with the stratified windy atmospheric profile of Fig. 1(a). For rays, the same color code is used as in Fig. 4. The green line is the sum of all ray contributions. The thin black line is the parabolic approximation computation (PE). Dashed line is the amplitude decay observed in a homogeneous atmosphere.

VII, corresponding respectively to stratospheric Is_d (zone III) and thermospheric It_d (zone VII) shadow zones, the exponential decay of amplitudes coincide almost perfectly, with the same slope, for both methods. The same spatial offset of slightly more than 1 km is observed as for real arrivals in zones IV and VIII. For the stratospheric shadow zone (zone IV, blue upward triangles), results coincide in the range 210-225.9 km, throughout approximately 16 km. For the thermospheric shadow zone (zone VII), results (red downward triangles) also coincide down to 355 km, throughout 7 km. Deeper inside this shadow zone (in zone VI) this diffracted field It_d vanishes, and the pressure field is dominated by real stratospheric fast arrivals Is_f. This comparison validates the method and algorithm developed in the present manuscript for implementing complex ray theory applied to infrasonic long-range propagation in an atmosphere with wind.

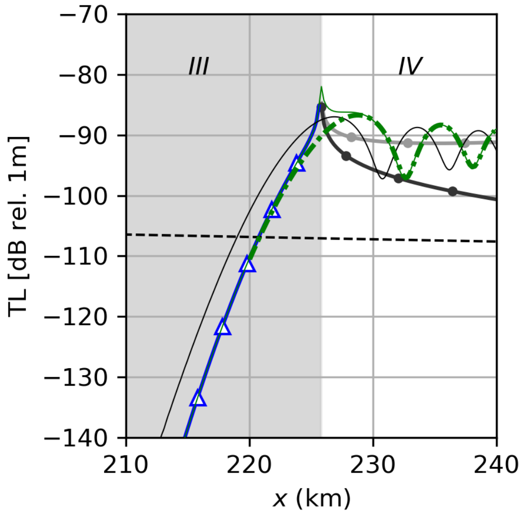

(a)

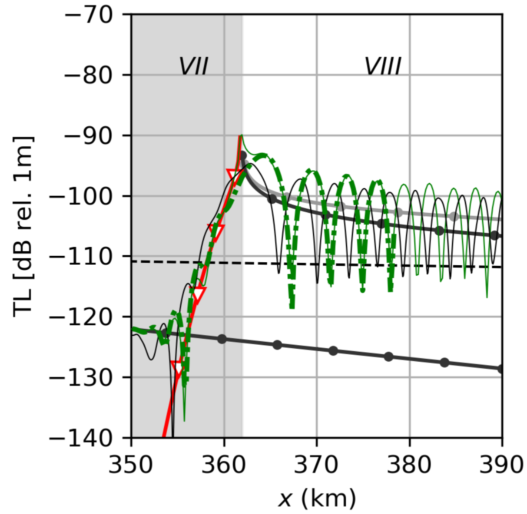

(b)

Fig. 6. (color inline) Same as Fig. 5 with zooms around the (a) stratospheric and (b) thermospheric caustics.

548 **D. Signatures**

549 In this section, we analyze waveform signatures in the illuminated and shadow zones
550 for the previous case of point source. The emitted signal at 1 m from the source $p_s(t) =$
551 $s(f(t-t_s))$ is a band limited frequency signal around the main frequency $f = 3\,\mathrm{Hz}$ defined
552 as:

$$s(\tau) = -0.5\sin(\pi\tau)\left[1+\cos(\pi\tau)\right], \tag{19}$$

553 for $\tau \in [-1,1]$ and $s(\tau) = 0$ otherwise. We display pressure signatures for stratospheric and
554 thermospheric arrivals in Fig. 7, obtained using complex ray tracing method. Geometrical
555 reduced arrival times of the mid-signal are indicated by the same color code as in previous
556 figures. Respective maxima of overpressure, noted $p_\star$, are indicated on the right with again
557 same color code. Considering $f = 3\,\mathrm{Hz}$, the results for stratospheric arrivals (Fig. 7(a)) have

similar shapes and reduced arrival times as in Blom (2019, Fig. 5) for receivers between 230 and 250 km.

Fast arrivals (black) keep the initial waveform $s(t)$ with an amplitude between 10^{-3} and 2.5×10^{-3} Pa. Slow arrivals corresponding to the Hilbert transform of the direct ones (Pierce, 1994), with an amplitude between 1.8×10^{-3} and 2.3×10^{-3} Pa. At the caustic, the two arrivals merge with a singular amplitude. In the shadow side, the single diffracted wave decreases exponentially with the distance from the caustic, with an amplitude of 3×10^{-4} at 220 km (i.e. 5.7 km from the caustic). As this decay is frequency dependent the signal loses its high frequency content and gets longer and asymetric.

For thermospheric arrivals (Fig. 7(b)), we observe a similar evolution with the distance. The amplitude of slow arrivals (gray) is noticeably smaller than those of fast arrivals. Note that stratospheric fast phases arriving much earlier and of very low amplitude.

In the shadow zone, such as the stratospheric ones, the amplitude decreases exponentially with an amplitude of 5.3×10^{-5} at 355 km (i.e. 6.8 km from the caustic).

VI. POINT SOURCE IN A WINDY AND RANGE DEPENDENT ATMOSPHERE

In this section, we consider the same point source located at (0,0) but with a range dependent atmosphere.

The singularity appearing in zone V in the previous case appears because the atmospheric data are range independent, thus allowing the ray launched horizontally to be refracted and reflects the ground again horizontally. According to catastrophe theory, this is not a full caustic as it is not structurally stable. For example, introducing range-dependent data

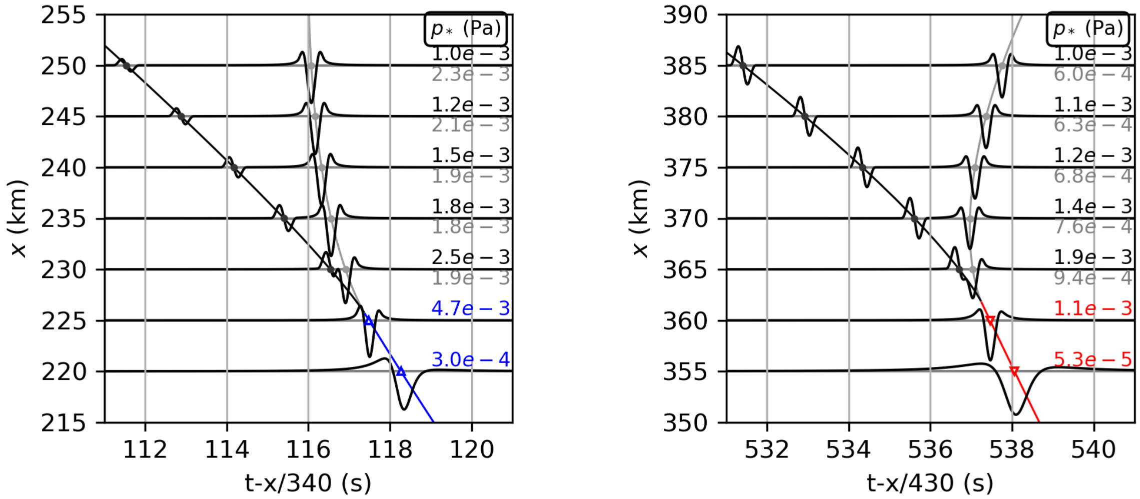

(a)

(b)

Fig. 7. (color inline) Time signatures around each caustics, for the incident wave defined by (19), for (a) stratospheric and (b) thermospheric arrivals, in the case of range-independent atmospheric profile.

should make this phenomenon disappear. The complex ray tracing method is perfectly adapted to simulate propagation in such an atmosphere. For comparison with the previous case, we keep the sound speed profile unchanged Lingevitch *et al.* (1999). The horizontal wind profile v is also a Gaussian function defined by Eq. (17), but now its amplitude $v_w(x)$ varies with range, decreasing linearly from 50 m/s at 0 km to -13 m/s at 500 km. The effective sound speed is shown in Fig. 8(a). The obtained stratospheric (Is_f, Is_s, Is_d) and thermospheric (It_f, It_s, It_d) rays are illustrated in Fig. 8(b) with same color code as for the range-independent case. Compared to this one, the slow-down of stratospheric jet tends to limit stratospheric refraction. In particular, with the same density of ground sensor, the number of slow stratospheric arrivals is sharply reduced. The position of the two caustics is consequently shifted, at distances of respectively 258.3 km (farther from the source than in

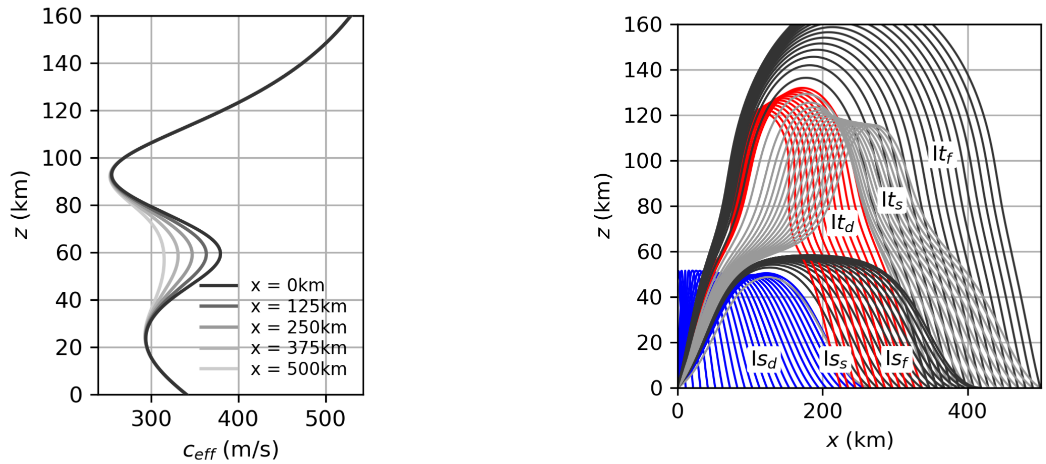

(a) (b)

Fig. 8. (color inline) (a) Range dependent effective sound speed profile $c_{\text{eff}} = c + v$. (b) Same as Fig. 3(a) for range dependent case.

the range independent case) for the stratospheric one, and 344.9 km (closer to the source) for the thermospheric one (see Fig. 8(b)).

Transmission losses are represented in Fig. 9 (with the same symbols and color codes as in Fig. 5). Seven zones, similar to those appearing in the range-independent case, can be observed, with the same types of arrivals. Only the former zone V, is no longer visible because the virtual caustic has disappeared. As a consequence, the main singularity of ray tracing method has been removed. When comparing with the numerical output of parabolic approximation, we observe that stratospheric (resp. thermospheric) ground arrivals are predicted by the parabolic simulation at shorter (resp. greater) distances than by ray tracing, with a difference of -1.1 km (resp. +4.4 km), (see Fig. 10). Except this offset, oscillations in zones IV and VII have the same shape for the two methods, but amplitudes differ by 2.6 dB in zone IV and by 2.3 dB in the zone VII. Inside stratospheric Is_d (zone III) and

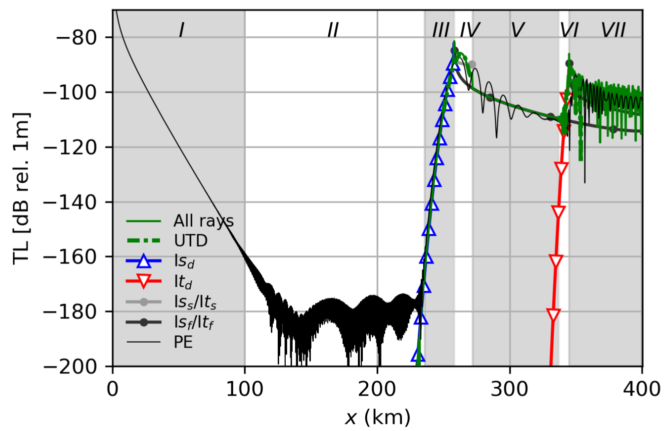

Fig. 9. (color inline) Same as Fig. 5 for range-dependent case.

thermospheric It_d (zone VI) shadow zones, the exponential decay of amplitudes coincide almost perfectly for both methods with the same offset as observed on the other side of the caustic. For the stratospheric shadow zone, results coincide in the range 236.8-258.3 km, throughout approximately 21 km. For the thermospheric shadow zone, the good matching is observed down to 336 km, throughout 8 km. Inside zone V the It_d contribution vanishes and the pressure field is dominated by real stratospheric fast arrivals Is_f only. Much better agreement between parabolic approximation and ray tracing is observed here compared to the equivalent zone VI in the range independent case, though field oscillations are not captured there by the ray tracing method. Similar as for the range-independent case, the UTD solution around stratospheric (Fig. 10(a)) and thermospheric (Fig. 10(b)) is represented with green dashed lines. The UTD maximum amplitude at the caustic agrees with the parabolic approximation one. The interference between the amplitude of the thermospheric caustic and the one of the Is_f ray is also well reproduce by UTD.

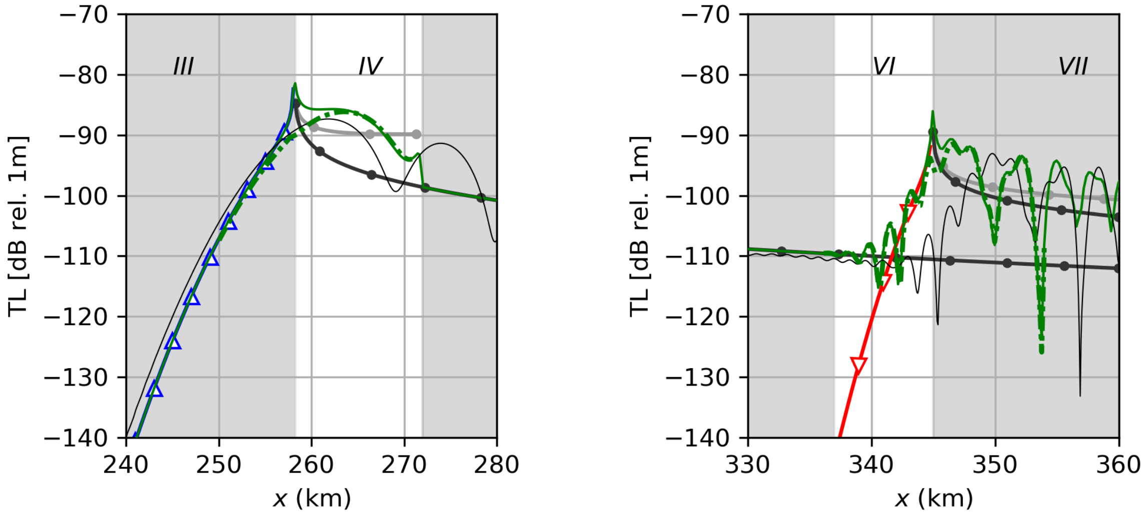

(a) (b)

Fig. 10. (color inline) Same as Fig. 9 with zooms on the (a) stratospheric and (b) thermospheric caustics.

VII. CONCLUSION

The objective of the present work was to implement complex ray theory and search for eigenrays in the case of infrasound propagation in stratified, and range dependent, atmospheres with wind. In particular, we wanted to capture diffraction around caustics. To our knowledge, complex ray theory has never been applied to infrasonic propagation. The method is appealing because it allows one to benefit from the efficiency of ray tracing even in shadow zones of caustics, where usual ray tracing methods fail. The key element of the method is the three stage algorithm developed to search for complex eigenrays between the source and the receiver. First, classical real ray shooting enables to identify caustics, shadow zones, bounds of waveguides and ground limited rays. Then, real interpolation and extrapolation in sonified zones, and complex extrapolation in the shadow zones, provides the initial guesses for the search of eigenrays expressed as an optimization process. This one is then solved by means of the Levenberg-Marquardt algorithm. The method has been validated by comparison with parabolic approximation for a stratified, and then for a range-dependent atmosphere. This comparison outlines the ability of the method to predict wave arrivals and amplitudes in the shadow zone of caustics.

The method nevertheless remains singular in tiny regions around caustics. This singularity is removed by a proper matching with the uniform theory of diffraction (Babich and Buldyrev, 1991; Felsen, 1984; Keller, 1962; Ludwig, 1966), using the universal field behavior around identified caustics.

Matching with other types of non-geometrical behavior, such as creeping waves, would need to be explored , along with extension of the method to three-dimensional cases, especially for meteorite sonic boom (Gainville *et al.*, 2017). Working with atmospheric data will also require to examine the proper interpolation of these data with analytical functions.

Amodei, D., Keers, H., Vasco, D., and Johnson, L. (**2006**). "Computation of uniform wave forms using complex rays.," Physical Review E **73**(3), 036704.

Assink, J., Waxler, R. and Velea, D. (**2017**). "A wide-angle high Mach number modal expansion for infrasound propagation," The Journal of the Acoustical Society of America **141**(3), 1781–1792.

Babich, V. M., and Buldyrev, V. S. (**1991**). *Short-wavelength diffraction theory: asymptotic methods* (Springer-Verlag).

Blixt, E. M., Näsholm, S. P., Gibbons, S. J., Evers, L. G., Charlton-Perez, A. J., Orsolini, Y. J., and Kværna, T. (**2019**). "Estimating tropospheric and stratospheric winds using infrasound from explosions," The Journal of the Acoustical Society of America **146**(2), 973–982.

Blokhintzev, D. (**1946**). "The propagation of sound in an inhomogeneous and moving medium I.," The Journal of the Acoustical Society of America **18**(2), 322–328.

Blom, P. and Waxler, R.(**2017**). "Modeling and observations of an elevated, moving infrasonic source: Eigenray methods," The Journal of the Acoustical Society of America **141**(4), 2681–2692.

Blom, P. (**2019**). "Modeling infrasonic propagation through a spherical atmospheric layer - Analysis of the stratospheric pair," The Journal of the Acoustical Society of America **145**(4), 2198–2208, doi: 10.1121/1.5096855.

Buchal, R.N. and Keller, J.B.(**1960**). "Boundary layer problems in diffraction theory," Commun. Pure Appl. Math **13**, 85–114.

Candel, S. (**1977**). "Numerical solution of conservation equations arising in linear wave theory: application to aeroacoustics," Journal of Fluid Mechanics **83**(3), 465–493.

Ceranna, L., Le Pichon, A., Green, D., and Mialle, P. (**2009**). "The buncefield explosion: a benchmark for infrasound analysis across central europe," Geophysical Journal International **177**(2), 491–508, doi: 10.1111/j.1365-246X.2008.03998.x.

Chapman, C. (**2004**). *Fundamentals of seismic wave propagation* (Cambridge University Press).

Chapman, S. J., Lawry, J. M. H., Ockendon, J. R., and Tew, R. H. (**1999**). "On the theory of complex rays," SIAM Review **41**(3), 417–509, doi: 10.1137/S0036144599352058.

Collins, M. D. (**1993**). "A split-step Padé solution for the parabolic equation method," The Journal of the Acoustical Society of America **93**(4), 1736–1742.

Courant, R., and Hilbert, D. (**2008**). *Methods of Mathematical Physics: Partial Differential Equations* (John Wiley & Sons).

de Groot-Hedlin, C. D., Hedlin, M. A., and Drob, D. P. (**2010**). "Atmospheric variability and infrasound monitoring," in *Infrasound Monitoring for Atmospheric Studies* (Springer), pp. 475–507.

Drob, D. P., Meier, R., Picone, J. M., and Garcés, M. M. (**2010**). "Inversion of infrasound signals for passive atmospheric remote sensing," in *Infrasound monitoring for atmospheric studies* (Springer), pp. 701–731.

Drob, D. P., Picone, J., and Garcés, M. (**2003**). "Global morphology of infrasound propagation," Journal of Geophysical Research: Atmospheres **108**(D21).

Egorchenkov, R. A., and Kravtsov, Y. A. (**2001**). "Complex ray-tracing algorithms with application to optical problems," Journal of the Optical Society of America A **18**(3), 650–656, doi: 10.1364/JOSAA.18.000650.

Evers, L., Van Geyt, A., Smets, P., and Fricke, J. (**2012**). "Anomalous infrasound propagation in a hot stratosphere and the existence of extremely small shadow zones," Journal of Geophysical Research: Atmospheres **117**(D6).

Farges, T., Hupe, P., Le Pichon, A., Ceranna, L., Listowski, C., and Diawara, A. (**2021**). "Infrasound thunder detections across 15 years over ivory coast: Localization, propagation, and link with the stratospheric semi-annual oscillation," Atmosphere **12**(9), 1188.

Felsen, L. (**1984**). "Geometrical theory of diffraction, evanescent waves, complex rays and Gaussian beams," Geophysical Journal International **79**(1), 77–88.

Gainville, O. (**2008**). "Modélisation de la propagation atmosphérique des ondes infrasonores par une méthode de tracé de rayons non linéaires," Ph.D. thesis, École centrale de Lyon, num. 2008-07.

Gainville, O., Henneton, M., and Coulouvrat, F. (**2017**). "A re-analysis of Carancas meteorite seismic and infrasound data based on sonic boom hypothesis," Geophysical Journal International **209**(3), 1913–1923, doi: 10.1093/gji/ggx122.

Gréa, B.-J., Luchini, P., and Bottaro, A. (**2005**). "Ray theory of flow instability and the formation of caustics in boundary layers," Technical Report.

Green, D. N., Waxler, R., Lalande, J.-M., Velea, D., and Talmadge, C. (**2018**). "Regional infrasound generated by the humming roadrunner ground truth experiment," Geophysical Journal International **214**(3), 1847–1864.

Hille, E. (**1997**). *Ordinary differential equations in the complex domain* (Courier Corporation).

Jensen, F. B., Kuperman, W. A., Porter, M. B., Schmidt, H., and McKay, S. (**1995**). *Computational Ocean Acoustics*, **9** (Modern Acoustics and Signal Processing), pp. 55–56.

Keller, J. B. (**1962**). "Geometrical theory of diffraction," J. Opt. Soc. Am. **52**(2), 116–130, doi: 10.1364/JOSA.52.000116.

Kendall, J., and Thomson, C. (**1993**). "Maslov ray summation, pseudo-caustics, lagrangian equivalence and transient seismic waveforms," Geophysical Journal International **113**(1), 186–214.

Kravtsov, Y. A. (**1967**). "Complex rays and complex caustics," Radiophys Quantum Electon **10**, 719–730, doi: doi.org/10.1007/BF01031601.

Kravtsov, Y. A., and Berczynski, P. (**2004**). "Description of the 2d Gaussian beam diffraction in a free space in frame of eikonal-based complex geometric optics," Wave Motion **40**(1), 23 – 27, doi: 10.1016/j.wavemoti.2003.12.012.

Kravtsov, Y. A., Forbes, G. W., and Asatryan, A. A. (**1999**). "I theory and applications of complex rays," Progress in Optics **39**, 1 – 62, doi: 10.1016/S0079-6638(08)70388-3.

Kravtsov, Y. A., and Orlov, Y. I. (**1983**). "Caustics, catastrophes, and wave fields," Soviet Physics Uspekhi **26**(12), 1038–1058, doi: 10.1070/pu1983v026n12abeh004582.

Kravtsov, Y. A., and Zhu, N. Y. (**2010**). *Theory of Diffraction. Heuristic Approaches* (Alpha Science International, United Kingdom).

Kulichkov, S., Bush, G. and Svertilov, A. (**2002**). "New type of infrasonic arrivals in the geometric shadow region at long distances from explosions," Izvestiya, Atmospheric and Oceanic Physics **38**(4), 397–402.

Kulichkov, S., Chunchuzov, I. and Popov, O. (**2010**). "Simulating the in- fluence of an atmospheric fine inhomogeneous structure on long-range propagation of pulsed acoustic signals," Izvestiya, Atmospheric and Oceanic Physics **46**(1), 60–68.

Kulichkov, S., and Golikova, E. (**2013**). "Nonlinear effects manifested in infrasonic signals in the region of a geometric shadow," Izvestiya, Atmospheric and Oceanic Physics **49**(1), 77–81.

Lalande, J.-M., Sèbe, O., Landès, M., Blanc-Benon, P., Matoza, R. S., Le Pichon, A., and Blanc, E. (**2012**). "Infrasound data inversion for atmospheric sounding," Geophysical Journal International **190**(1), 687–701.

Lalande, J.-M. and Waxler, R. (**2016**). "The interaction between infrasonic waves and gravity wave perturbations: Application to observations using UTTR rocket motor fuel elimination events," Journal of Geophysical Research: Atmospheres **121**(10), 5585–5600.

Le Pichon, A., Blanc, E., and Hauchecorne, A. (**2010**). *Infrasound monitoring for atmospheric studies* (Springer Science & Business Media).

Lingevitch, J. F., Collins, M. D., and Siegmann, W. L. (**1999**). "Parabolic equations for gravity and acousto-gravity waves," The Journal of the Acoustical Society of America **105**(6), 3049–3056, doi: 10.1121/1.424634.

Ludwig, D. (**1966**). "Uniform asymptotic expansions at a caustic," Communications on Pure and Applied Mathematics **19**(2), 215–250.

Moré, J. J. (**1978**). "The levenberg-marquardt algorithm: implementation and theory," in *Numerical analysis* (Springer), pp. 105–116.

Nguyen-Dinh, M., Gainville, O., and Lardjane, N. (**2018**). "A one-way coupled euler and parabolic model for outdoor blast wave simulation in real environment," Journal of Theoretical and Computational Acoustics **26**(04), 1850019.

Ostashev, V., and Wilson, D. K. (**2015**). *Acoustics in moving inhomogeneous media* (CRC Press).

Pierce, A. D. (**1994**). *Acoustics : An Introduction to Its Physical Principles and Applications* (Acoustical Society of America), p. 371.

Pierce, A. D., and Maglieri, D. J. (**1972**). "Effects of atmospheric irregularities on sonic-boom propagation," The Journal of the Acoustical Society of America **51**(2C), 702–721.

Piserchia, P.-F. (**1998**). "Propagation et conversion des ondes t par simulation numerique hydride," Ph.D. thesis, Thèse de doctorat dirigée par Virieux, Jean Terre, océan, espace Nice 1998, 1998NICE5175.

Porter, M. B., and Bucker, H. P. (**1987**). "Gaussian beam tracing for computing ocean acoustic fields," The Journal of the Acoustical Society of America **82**(4), 1349–1359.

Press, W. H., Flannery, B. P., Teukolsly, S. A., and Vetterling, W. T. (**1996**). *Numerical Recipies in Fortran 90* (Cambridge University Press, Cambridge, UK).

Sabatini, R., Marsden, O., Bailly, C., and Gainville, O. (**2019**). "Three-dimensional direct numerical simulation of infrasound propagation in the earth's atmosphere," Journal of Fluid Mechanics **859**, 754–789.

Scott, J., Blanc-Benon, P., and Gainville, O. (**2017**). "Weakly nonlinear propagation of small-wavelength, impulsive acoustic waves in a general atmosphere," Wave Motion **72**, 41 – 61, doi: 10.1016/j.wavemoti.2016.12.005.

Stone, J. T., Self, R. H., and Howls, C. J. (**2018**). "Cones of silence, complex rays and catastrophes: high-frequency flow–acoustic interaction effects," Journal of Fluid Mechanics **853**, 37–71, doi: 10.1017/jfm.2018.544.

Thom, R. (**1983**). *Mathematical models of morphogenesis* (Ellis Horwood).

Thomson, C., and Chapman, C. (**1985**). "An introduction to maslov's asymptotic method," Geophysical Journal International **83**(1), 143–168.

Thomson, C. J. (**1997**). "Complex rays and wave packets for decaying signals in inhomogeneous, anisotropic and anelastic media," Studia Geophysica et Geodaetica **41**(4), 345–381.

Transtrum, M. K., and Sethna, J. P. (**2012**). "Improvements to the levenberg-marquardt algorithm for nonlinear least-squares minimization," Journal of Computationl Physics .

Vanderbecken, P., Mahfouf, J.-F., and Millet, C. (**2020**). "Bayesian selection of atmospheric profiles from an ensemble data assimilation system using infrasonic observations of may 2016 mount etna eruptions," Journal of Geophysical Research: Atmospheres **125**(2), e2019JD031168.

Virieux, J., Garnier, N., Blanc, E., and Dessa, J.-X. (**2004**). "Paraxial ray tracing for atmospheric wave propagation," Geophysical Research Letters **31**(20), doi: 10.1029/2004GL020514.

Waxler, R., Läslo, G., Assink, J., and Blom, P. (**2015**). "The stratospheric arrival pair in infrasound propagation," The Journal of the Acoustical Society of America **137**(4), 1846–1856.

White, D. W., and Pedersen, M. A. (**1981**). "Evaluation of shadow-zone fields by uniform asymptotics and complex rays," The Journal of the Acoustical Society of America **69**(4), 1029–1059.

Whitham, G. (**1956**). "On the propagation of weak shock waves," Journal of Fluid Mechanics **1**(3), 290–318.

Wu, J., Zhou, B., Li, X., and Bouzidi, Y. (**2021**). "Effective and efficient approaches for calculating seismic ray velocity and attenuation in viscoelastic anisotropic media," GEOPHYSICS **86**(1), C19–C35, doi: 10.1190/geo2020-0126.1.